Analyst

Accepted Manuscript

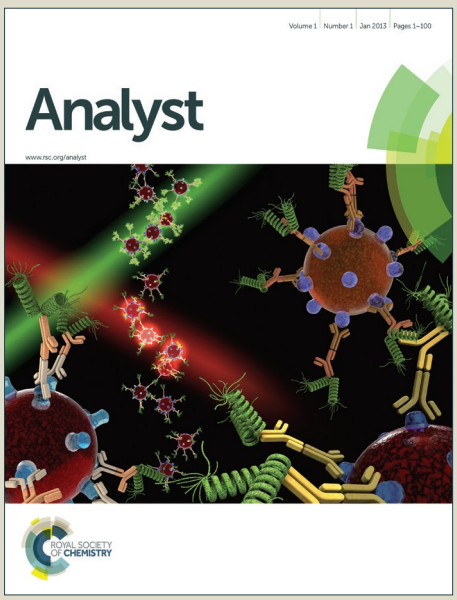

ROYAL SOCIETY OF CHEMISTRY

www.rsc.org/analyst

Cite this: DOI: 10.1039/c0xx00000x

www.rsc.org/xxxxxx

ARTICLE TYPE

Supramolecular recognition control of polyethylene glycol modified N-doped graphene quantum dots: tunable selectivity for alkali and alkaline-earth metal ions

Siwei Yang, Jing Sun, Chong Zhu, Peng He, Zheng Peng and Guqiao Ding, *

Received (in XXX, XXX) Xth XXXXXXXXX 20XX, Accepted Xth XXXXXXXXX 20XX
DOI: 10.1039/b000000x

The graphene quantum dot based fluorescent probe community needs unambiguous evidences about the control on the ion selectivity. In this paper, polyethylene glycol modified N-doped graphene quantum dots (PN-GQDs) were synthesized by alkylation reaction between graphene quantum dots and organic halides. We demonstrate the tunable selectivity and sensitivity by controlling the supramolecular recognition through the length and end group size of polyether chain on PN-GQDs. The relationship formulas between selectivity/detection limit and polyether chains are experimentally deduced. The polyether chain length determines the interaction between PN-GQDs and ions with different ratios of charge to radius, which in turn leads to a good selectivity control. Meanwhile the detection limit shows exponential growth with size of end groups of polyether chain. The PN-GQDs can be used as ultrasensitive and selective fluorescent probes for Li^+, Na^+, K^+, Mg^{2+}, Ca^{2+} and Sr^{2+}, respectively.

Introduction

Alkali and alkaline-earth metal ions (such as: Li^+, Na^+, K^+, Mg^{2+}, Ca^{2+} and Sr^{2+}) are the most important ions in physiological activities. [1-5] Active transportation is responsible for cells containing relatively high concentrations of K^+ but low concentrations of Na^+. [6-8] A sodium-potassium pump that moves both Na^+ and K^+ in opposite directions across the plasma membrane is responsible for the mechanism of the ion transportation. [8-13] The concentrations of Na^+ and K^+ on opposite sides of membrane are interdependent, suggesting that the same carrier transports both ions. On the other hand, Mg^{2+} and Ca^{2+} play key roles in nerve transmission, maintenance of muscular strength and extracellular osmolarity, enzyme activation, apoptosis of a cell, regulation of blood pressure, pH, and the concentration of other ions in living cells. [14-17] Abnormal Mg^{2+} and Ca^{2+} concentration is a symptom of several diseases, including kidney diseases, heart disease, diabetes and cancer. [14-19] Moreover, Sr^{2+} is also one of essential microelements for people and animal. Currently, "On-Off" fluorescent probe is widely used for ion detection. The quench mechanism of most "On-Off" fluorescent probes depends on the supramolecular interaction (mainly coordination or hydrogen-bond interaction) between supramolecular donors (ions) and acceptors (functional groups of probes). [20-23] However, since the supramolecular interaction between Alkali/alkaline-earth metal ions and fluorescent probes is very week, the design and preparation of fluorescent probes for these ions is much harder than that for transition metal ions (such as: Cu^{2+}, Ag^+ and Fe^{3+}). [14, 16]

Supramolecular interaction depends on the surface of fluorescent probe, and graphene quantum dots (GQDs) is a "pure surface" materials due to its special two-dimensional sp^2-bonded structure with only one or two atomic layer thickness. [24-29] The GQDs can be modified or doped with abundant functional groups, which is suitable for supramolecular recognition with high efficiency. [28] Thus, GQDs are considered as a promising photoluminescence (PL) material for fluorescent probe. [30-37] Yang *et al*. designed the fluorescent switch for the detection of oxidative hydroxyl radical and reductive glutathione based on the use of selenium doped GQDs. [33] Other researchers also reported the GQDs based fluorescent probes (such as: Cu^{2+}, Hg^{2+} and Ag^+). [34-39] The excellent performance and extensive application prospect of GQDs result in the requirements of diversified GQD based fluorescent probes. But the most fundamental problem of developing GQD based fluorescent probes is how to control their selectivity. We have demonstrated the change of selectivity in N or S doped carbon based quantum dots. [2] Unfortunately, to our knowledge, for different ions, there is still no specific direction for the selectivity control of GQD based fluorescent probes. The GQDs community needs unambiguous evidences about the control of functional group, and its effect on supramolecular recognition or selectivity.

In this paper, polyethylene glycol modified N doped graphene quantum dots (PN-GQDs) were synthesized by alkylation reaction between N doped graphene quantum dots and organic halides. We demonstrate the tunable supramolecular recognition of PN-GQDs. The supramolecular interaction between polyether chains and ions results in the static quenching of PN-GQDs. The length of polyether chains decides the selectivity of PN-GQDs which conforms to logarithmic relationship with the ratio of charge to radius of ions. Meanwhile, the detection limit shows

exponential growth with end group size of polyether chains. With tunable chain length of polyethylene glycol the PN-GQDs can be used as ultrasensitive and selective fluorescent probes for Li^+, Na^+, K^+, Mg^{2+}, Ca^{2+} and Sr^{2+} with high stability, respectively.

Methods

Synthesis of N-GQDs

N-GQDs were synthesized as follows: the second oxidation graphene oxide (GO) [27] was dissolved in DMF with the concentrations of 10 mg mL^{-1}. The GO/DMF solutions were under ultrasonication for 1h (200 W, 100 kHz) to obtain homogeneous dispersion system. The GO/DMF solutions were transferred to a Teflon-lined autoclave (50 mL) and heated at 200 ^oC for 4 h, and cooling to room temperature naturally. The product was filtered by 0.02 μm microporous membrane and a brown transparent filter solution was contained. The detailed preparation process can be referenced to the Ref. 27.

Synthesis of PN-GQDs

PN-GQDs were synthesis via the alkylation reaction between N doped graphene quantum dots and different organic halides (experiment details in supplementary information). Typically, the synthesis progress of PN-GQD-1 is shown in Figure 1a and as follows: 12.4 mg (0.1 mM) 2-Methoxyethoxymethyl chloride was added into 9.0 mL, 1.0 mg mL^{-1} N-GQDs aqueous solution. The mixture were transferred to a Teflon-lined autoclave (10 mL) and heated at 180 ^oC for 24 h. The obtained aqueous solution was dialysed in a 3500 Da dialysis bag for a week to remove small molecules.

Characterization methods

Transmission electron microscopy (TEM) measurements were carried out on a spherical aberration-corrected TEM (FEI Titan 80-300) at 80 kV. X-ray photoelectron spectra (XPS) were carried out on a PHI Quantera II system (Ulvac-PHI, INC, Japan). The UV-vis spectra were obtained on a UV5800 Spectrophotometer. PL and PLE spectra were recorded on a PerkinElmer LS55 luminescence spectrometer (PerkinElmer Instruments, U.K.) at room temperature in aqueous solution. The stability of these products was determined via contrast the fluorescent emission intensity of products aqueous solution under different conservative time at room temperature. The Hela cell line was obtained from the Cell Bank of Chinese Academy of Science and cultured in the standard medium at 37 °C in 5% CO_2. Cells were seeded in a 96-well plate for 24 h before GQDs treatment. Serial dilutions of GQDs with known concentrations were added into cells. After 24 h incubation, the relative viabilities of cell samples were determined by colorimetric 3-(4,5-dimethylthiazol-2-yl)-2,5-diphenyl tetrazolium bromide (MTT) assays were performed to assess the metabolic activity of cells treated as described above.

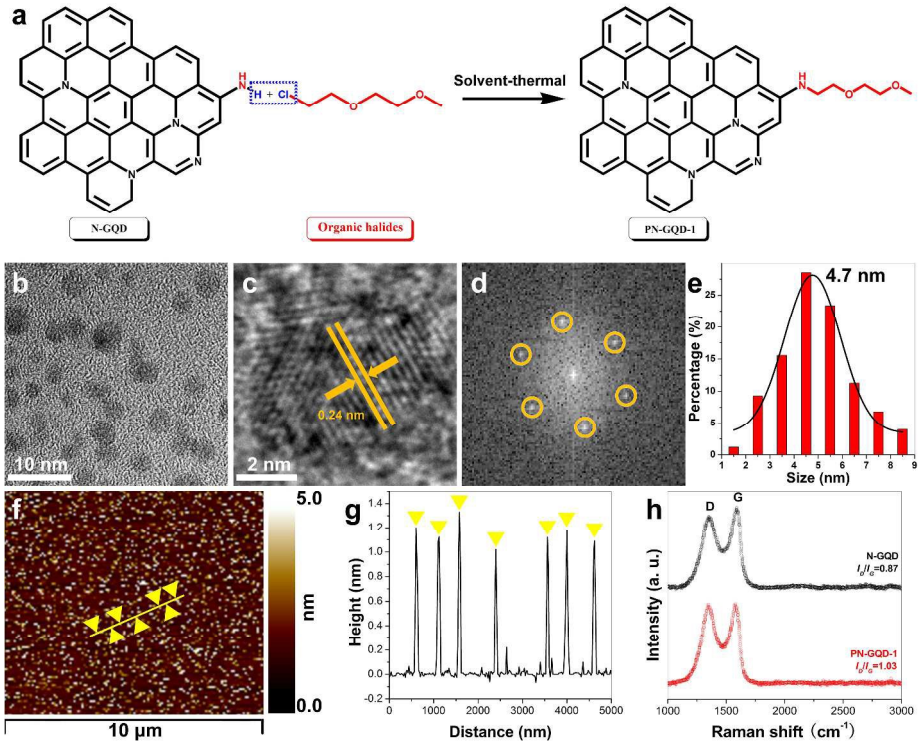

Figure 1 (a) Schematic diagram of the preparation process. PN-GQD-1 was obtained by solvent-thermal treatment of the mixture of N-GQDs and 2-methoxyethoxymethyl chloride. (b) TEM image of PN-GQD-1, (c) High-resolution TEM image of a single PN-GQD-1 dot, (d) FFT of a single dot in c. (e) corresponding size distribution histogram of PN-GQD-1, the black curve is the Gaussian fitting curve. (f) AFM topography images of PN-GQD-1 on a mica substrate in tapping mode with the Bruker Dimension Icon AFM microscope, (g) height profile analysis along the line in the AFM image. (h) Raman spectrum of N-GQDs (black curve) and PN-QD-1 (red curve).

Results and discussion

Structural characterization

The low magnification TEM image of the as-obtained PN-GQD-1 is shown in Figure 1b. TEM image indicates monodispersed PN-GQD-1 dots. The High-resolution TEM (HTEM) image shows PN-GQD-1 have crystallinity with lattices of 0.24 nm (Figure 1c). The lattices can be attributed to the (1120) lattice fringe of sp^2 clusters in PN-GQD-1. [40] Fast Fourier transform (FFT) (Figure 1d) shows a high crystalline structure and significant non-standard six-fold symmetry, which further indicating the graphene structure of PN-GQD-1. [27] The size distribution of PN-GQD-1 was evaluated from the TEM image by measuring about 150 individual dots. As shown in Figure 1e, the diameter of the quantum dots ranges from 1.5 to 8.5 nm and mainly locates at 4.7 nm. The size distribution exhibits no obvious change after modification (the diameter of the N-GQDs ranges from 1.6 to 7.8 nm and mainly locates at 4.4 nm, see Figure S1). Moreover, the suitable size distribution of PN-GQD-1 endows them with the possibility to enter the cellular nucleus. Atomic force microscope (AFM) observations (Figure 1 f and g) reveal highly dispersed PN-GQD-1 on the mica substrate with a typical topographic height of 0.9-1.3 nm, which indicates the 1-2 atomic layers in thickness. [41]

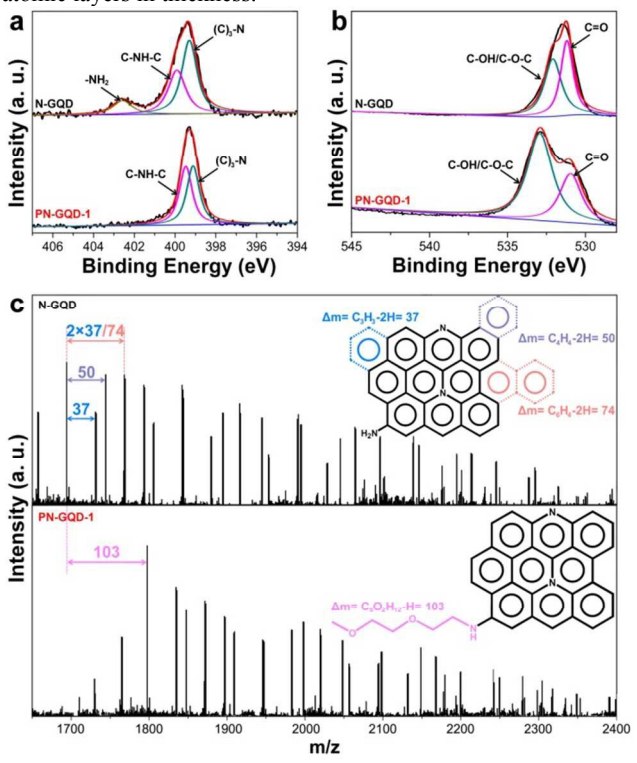

Figure 2 High-resolution (a) N 1s and (b) O1s spectrum of N-GQDs and PN-GQD-1. (c) MALDI-TOF mass spectra of N-GQD and PN-GQD-1. Note that peaks are detected as Na ion adducts ($[M+Na]^+$), the Na^+ of which might have originated from residue in the reagents used for graphite oxidation to prepare the graphene oxide.

Raman spectra of PN-GQD-1 and N-GQDs are carried out (Figure 1h) to demonstrate the structure change. The Raman spectra of carbon materials, D (*ca.* 1350 cm^{-1}) and G (*ca.* 1590 cm^{-1}) bands [41] are characteristic signals. In the graphene-based materials, G band is corresponding to the sp^2 hybridized carbon atoms in the hexagonal framework, and D band is indicative of sp^3 hybridized carbon atoms on the defects and edges of the graphene sheets. [41] The obtained PN-GQD-1 have higher D/G intensity ratio (I_D/I_G= 1.03) than N-GQDs (I_D/I_G= 0.87) indicates the increased sp^3 hybridized carbon atoms which can be due to the sp^3 hybridized carbon atoms of polyethylene glycol chains.

Fourier Transform infrared spectroscopy (FT-IR) and X-ray photoelectron spectroscopy (XPS) were undertaken to probe surface groups of PN-GQD-1. FT-IR spectrum of PN-GQD-1 (Figure S2) shows the peak located at 1150 cm^{-1} corresponding to the signals of C-O-C groups which can be due to the ether bonds of epoxy groups and polyether chain in PN-GQD-1. [42] The peak located at 2917, 1645 and 1055 cm^{-1} corresponding to the signals of C=O, C=C, and C-O groups of PN-GQD-1. The peak located at 3435 corresponding to the signals of $-NH_2$ groups in N-GQDs. This indicates the reducing of $-NH_2$ groups in modification progress. These diversified oxygen-containing groups result in the dispersibility of PN-GQD-1. XPS was undertaken to probe the change of surface groups of N-GQDs and PN-GQD-1. The XPS survey spectra for N-GQDs and PN-GQD-1 both show a C 1s peak at ca. 284.2 eV, along with an O 1s peak at ca. 532 eV and an N 1s peak at ca. 399 eV (Figure S3). The atomic ratio of C, O and N in N-GQDs is 83.3, 6.2 and 10.5 at. %, respectively (Table S1). The nitrogen content of PN-GQD-1 is similar with N-GQDs (10.7 at. %) indicating the good stability of nitrogen-containing groups in these quantum dots. However, the oxygen content of PN-GQD-1 is lower than N-GQDs (8.5 at. %) which can be due to the decomposing of oxygen-containing groups in solvent-thermal progress.

Figure 2a shows the well-fitted N 1s spectra of N-GQDs and PN-GQD-1. The N 1s spectrum of N-GQDs can be divided into three different peaks. The peaks located at 402.1, 400.2 ad 399.4 eV are corresponding to the signals of amino groups, parahelium groups and aromatic N. [27, 43-45] The proportion of amino groups ($-NH_2$), parahelium groups (C-NH-C) and aromatic N ($(C)_3$-N) is 15%, 28% and 57%, respectively. However, the signal of amino groups is unobservable in N 1s spectrum of PN-GQD-1. The expending of amino groups can be attributed to the alkylation reaction between amino groups and organic halides (Figure 1a). At the same time, the proportion of parahelium groups of PN-GQD-1 increased (51%) which can be summed up to the additional generated parahelium in alkylation reaction. It deserved to note that, due to the large steric hindrance of N-GQDs, the additional generated tertiary amine can't obtained in this alkylation reaction. The O 1s spectrum (Figure 2b) of N-GQDs can be divided into two different peaks, which correspond to the signals of C-OH/C-O-C (533.4 eV) and C=O (532.4 eV). [43-45] The proportion of C-OH/C-O-C and C=O is 38% and 64%, respectively. The proportion significantly changed after modification. As shown in Figure 2b, the proportion of C-OH/C-O-C of PN-GQD-1 increased (72%) which is much higher than N-GQDs. The additional ether bonds in polyether chains result in this change.

Finally, the MALDI-TOF-MASS spectra were carried out to further characters molecular structure of PN-GQD-1. Figure 4e shows the MALDI-TOF-MASS spectrum of N-GQDs and PN-

GQDs. The MALDI-TOF-MASS spectrum of N-GQDs shows the peaks at m/z of 1800-2400 (Figure 2c) indicating 80-120 aromatic nucleuses in single N-GQD which match the TEM results. Because of the 'non-selective' fragmentation of N-GQDs preparation progress, the repeating unit of m/z 37, 50 and 74 to the reflection of their edge structures can be observed (Figure 2c inset). [46] The repeating unit of m/z 37 expected to be a six-membered carbon ring bonded to a zigzag edge of an N-GQD (schematically shown in blue part the inset of Figure 2c inset). On the other hand, the mass of 50 and 74 are expected to be a six-membered C ring bonded to an armchair edge of an N-GQD (schematically shown in violet and red part the inset of Figure 2c inset). [47]

On the other hand, the mass pattern from PN-GQD-1 shifted to a higher mass by precisely m/z 103. Meanwhile, the mass pattern retained the regularity of the repeating m/z 37, 50 and 74 unit, as shown in Figure 2c. The difference of m/z 103 can be attributable to the attachment of additional functional groups by forming N-C bond (doubly confirmed by FT-IR and XPS analysis) between amino group groups and carbon-halogen bonds (C-Cl).

Optical properties

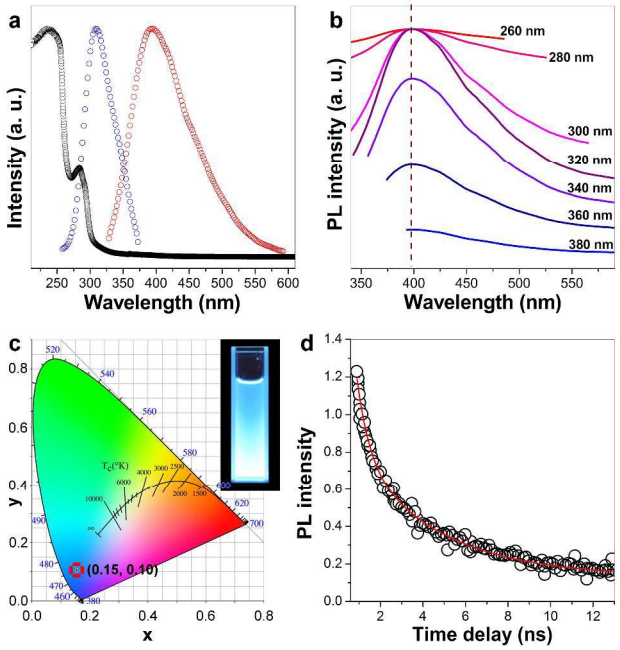

Figure 3 (a) Normalized UV-vis absorption (black curve), PL (red curve) and PLE (blue curve) spectra of PN-GQD-1 aqueous solution. (b) PL spectra of PN-GQD-1 aqueous solution under different excitation conditions (λ_{ex}= 260, 280, 300, 320, 340, 360 and 380 nm, respectively). (c) The CIE chromaticity coordinates for PN-GQD-1 in aqueous solution. Inset: digital image of GQD aqueous solution (2.0 mg mL^{-1}) under UV-light (the centre wavelength of UV-light is 365 nm). (d) PL decay curve and fitting curve of PN-GQD-1 measured at room temperature with λ_{ex} at 321 nm.

The optical properties of PN-GQD-1 are shown in Figure 3. The UV-vis absorption spectrum of PN-GQD-1 (Figure 3a) shows a typical π-π* transition absorption peak (due to the of aromatic sp^2 domains) around 258 nm, an n-π* transition absorption peak around 280 nm, and a long tail extending into the visible range. [47] The strong and sharp PL emission peak (red curve in Figure 3a) at 402 nm can be observed at an excitation wavelength (λ_{ex}) of 321 nm. The emission wavelength (λ_{em}) of PN-GQD-1 has no obvious change, compared with N-GQDs (λ_{em}= 408 nm, Figure S4). This can be due to the week conjugation of N-C bond. [32, 33, 38] The full-width at half-maximum of PL peak is 90 nm and the φ is 0.71. The high φ can be due to the unitary PL progress of n-π* transition of aromatic N in PN-GQD-1. [27] The unitary PL progress also results in the excitation wavelength independent of PN-GQD-1. As shown in Figure 3b, when the λ_{ex} shift from 260 to 380 nm, the λ_{em} shows no obvious shift. The Commission International d'Eclairage (Figure 3c) chromaticity coordinates for PN-GQD-1 is (0.15, 0.10) indicates the obtained PN-GQD-1 emits blue PL. Indeed, as shown in Figure 3c inset, the PN-GQD-1 aqueous solution gives bright blue PL under UV-light.

The PL decay of PN-GQD-1 is measured by a time-correlated single photon counting technique, and fitted well with a bi-exponential decay as shown in Figure 3d. The lifetime (τ) is dominated by a long decay component of 8.4 ns (94%) plus a small contribution from the short decay of 1.3 ns (7%), the weighted-average lifetime is approximately 8.0 ns. The long PL lifetime also explains the high quantum yield observed in this PN-GQD-1. [27] To combine the φ and τ by κ_r=φ/τ we can obtain the radiative rates κ_r. [48, 49] The fluorescence radiative rate κ_r of PN-GQDs is 8.88×10^7 s^{-1}.

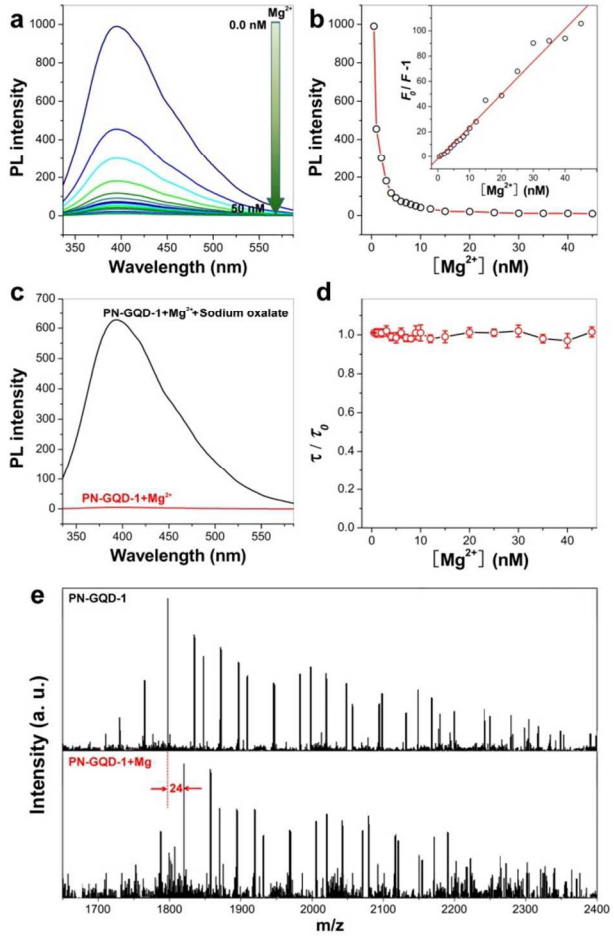

Figure 4 (a) PL spectra and (b) PL intensity of PN-GQD-1 versus different Mg^{2+} concentrations (from 0.5 to 50 nM). Inset of Figure 4b: Stern–Volmer plot PN-GQD-1 versus different Mg^{2+} concentrations. The concentration of PN-GQD-1 is 0.2 mg mL^{-1}. (c) PL spectra of PN-GQD-1

and Mg^{2+} system. The black and red curves for PL spectra with and without sodium oxalate, respectively. (d) τ of PN-GQD-1 plotted against the concentration of Mg^{2+}, where τ_0 and τ are the PL lifetimes in the absence and presence of Mg^{2+}, respectively. (e) MALDI-TOF mass spectra of PN-GQD-1 in the absence and presence of Mg^{2+}, respectively. Note that peaks are detected as Na ion adducts ($[M+Na]^+$), the Na^+ of which might have originated from residue in the reagents used for graphite oxidation to prepare the graphene oxide.

We explored the feasibility of PN-GQDs for the detection of Mg^{2+}. The dramatic PL quenching behavior of PN-GQD-1 can be observed when Mg^{2+} ($Mg(NO_3)_2$) is added into the solution (Figure 4a). It is obvious that the PL intensity decreases as more Mg^{2+} is added. The fluorescence quenching data follow the equation E1 and as follows:

$$F_0 / F = 1 + K \times [Q] \quad \text{(E1)}$$

where [Q] is the analyte (Mg^{2+}) concentration, and F_0 and F are PL intensities of PN-GQDs at 402 nm in the absence and presence of Mg^{2+}, respectively. [50] The plot shown in the inset of Figure 2b fits a linear in the concentration range of 5×10^{-10} to 5×10^{-8} M. The correlation coefficient (R^2) and K are 0.9898 and 2.5839 determining Mg^{2+}, respectively. The detection limit is estimated to be 2×10^{-10} M at a signal-to-noise ratio of 3.

We further confirmed the quencher by ion capture test, when an Mg^{2+} precipitant (such as sodium oxalate) is added, Mg^{2+} is removed from the surface of PN-GQD-1 by forming sediment (magnesium oxalate), which results in the PL recovery of PN-GQD-1 (Figure 4c). This efficient PL recovery strongly conform Mg^{2+} is the quencher in above sensing progress.

Lifetime measurements of PN-GQD-1 with different amounts of quencher (Mg^{2+}) were carried out for evidence of the quenching mechanism. In static quenching, the τ does not change (τ_0 / τ=1) as the molecules where τ_0 and τ are the fluorescence lifetimes in the absence and presence of quencher, respectively. [2, 51] This does not form a complex with the quencher in the ground state having the original lifetime (τ_0). The quenching process can be due to the supramolecular interaction between PN-GQD-1 and quencher. On the other hand, in dynamic quenching, $F_0 / F = \tau_0 / \tau$, and the lifetime decreases on addition of the quencher. [2, 52] Figure 3d shows typical results for the effect of quencher concentration on the lifetime of PN-GQDs. The τ of PN-GQDs did not change (τ_0/τ= 1) upon Mg^{2+} addition suggesting that the quenching behavior is due to the static quenching process. Thus, the supramolecular interaction between Mg^{2+} and PN-GQD-1 results in the static quenching behavior during the sensing progress.

Moreover, the complex compound was caught by MALDI-TOF-MASS spectrum. As shown in Figure 4e, the mass pattern from PN-GQDs shifted to a higher mass by precisely m/z 24 which indicates the complex compound of PN-GQDs and Mg^{2+}. Meanwhile, the mass pattern retained the regularity of the repeating m/z 37, 50 and 74 unit. Moreover, the coordination ratio is 1:1 and the binding site is the polyether chain in PN-GQDs.

Finally, the control experiment is used to confirm the binding site of above supramolecular interaction. As shown in Figure S5, the PL intensity of N-GQDs showed no change when the Mg^{2+} was added. This means the polyether chains is the acceptor in supramolecular interaction progress between Mg^{2+} and PN-GQD-1.

Next, based on above results, the PN-GQDs with different polyether chains were prepared to understand and further control the supramolecular interaction between PN-GQDs and metal ions. As shown in Figure 5a, the number of chain length of polyether chain (the number of ethylene glycol units, n_{pc}) in PN-GQD-2, PN-GQD-3, PN-GQD-4, PN-GQD-5 and PN-GQD-6 is 3, 4, 5, 6 and 7, respectively. TEM images and PL spectrum are shown in Figure S6 and 7. The PL fluorescence properties of these PN-GQDs are shown in Figure S8 and Table 1. The λ_{ex} and λ_{em} of these PN-GQDs are *ca.* 320 and *ca.* 400 nm, respectively. All these PN-GQDs show high quantum yield which is *ca.* 0.7.

The dramatic PL quenching behavior of PN-GQD-2, PN-GQD-3, PN-GQD-4, PN-GQD-5 and PN-GQD-6 can be observed when Ca^{2+}, Sr^{2+}, Li^+, Na^+ and K^+ is added. As shown in Figure 5b, when the concentration of corresponding ions is 50 nM, the dramatic PL quenching of PN-GQDs can be observed. The PL intensity decreased to the 1% of original intensity (F_0 /F -1 is larger than 100). The detection limit of PN-GQD-2, PN-GQD-3, PN-GQD-4, PN-GQD-5 and PN-GQD-6 is 0.1, 0.4, 0.5, 0.1 and 0.3 nM, respectively (at a signal-to-noise ratio of 3).

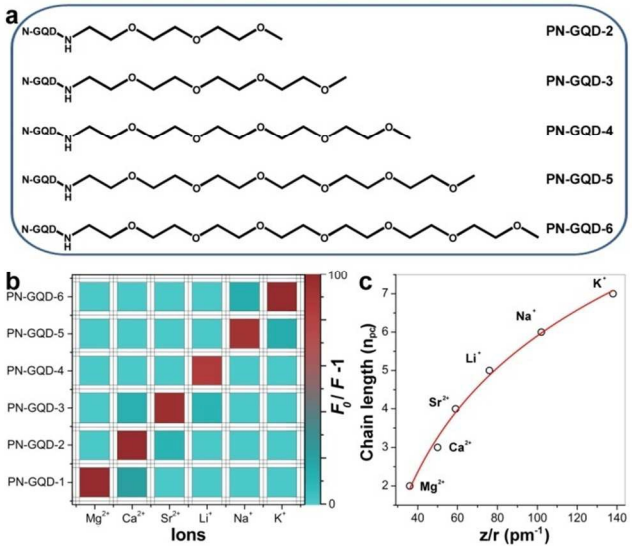

Figure 5 (a) molecular structures of PN-GQDs with different polyether chains. (b) PL response of PN-GQD-1, PN-GQD-2, PN-GQD-3, PN-GQD-4, PN-GQD-5 and PN-GQD-6 for different alkali and alkaline-earth metal ions. The concentration of PN-GQDs and ions is 0.2 mg mL^{-1} and 50 nM, respectively. (c) Relationship between chain length of polyether chain in PN-GQDs and the ratio of charge to radius of ions. The red curve shows the logarithm fitting curve.

These PN-GQDs also show high selectivity. Taking PN-GQD-2 as an example (Figure 5b), the PL intensity show no change when Mg^{2+}, Sr^{2+}, Li^+, Na^+ and K^+ were added (F_0 / F -1= 0). The selectivity for similar alkali and alkaline-earth metal ions is so remarkable which is much better than crown ethers. [53-55] This exact selectivity and supramolecular recognition imply the potential relationship between polyether chains and substantive characteristics of alkali and alkaline-earth metal ions. Figure 5c shows the relationship between the n_{pc} and the ratio of charge to radius (z/r) of ions. It is clear that with the increasing of z/r, the n_{pc} increased nonlinearly which meet well with the logarithmic relationship (as shown in red curve of Figure 5c). The fitting formula is shown in E2 and the correlation coefficient (R^2) is 0.9994.

n_{pc}= -9.894+3.478×ln[(z/r)-6.132] (E2)

This result indicates the selectivity of PN-GQDs depends on the n_{pc}. The PN-GQDs with longer polyether chains can be used as fluorescent probes for the ions with larger z/r.

Table 1 The λ_{ex}, λ_{em}, φ, τ and detection limit of N-GQDs, PN-GQD-1, PN-GQD-2, PN-GQD-3, PN-GQD-4, PN-GQD-5, PN-GQD-6, PN-GQD-1B, PN-GQD-1C and PN-GQD-1D.

	λ_{ex} (nm)	λ_{em} (nm)	φ [a]	τ (ns)	Detection limit (nM)
N-GQD	321	408	0.74	9.2	
PN-GQD-1	321	402	0.71	8.0	0.2
PN-GQD-2	318	400	0.73	7.6	0.1
PN-GQD-3	322	405	0.69	8.8	0.4
PN-GQD-4	321	399	0.72	7.4	0.5
PN-GQD-5	322	402	0.71	8.2	0.1
PN-GQD-6	321	405	0.71	7.8	0.3
PN-GQD-1B	318	402	0.70	8.3	0.4
PN-GQD-1C	216	405	0.71	7.6	0.9
PN-GQD-1D	318	402	0.71	7.9	8.1

[a] Quininesulfate as a standard (φ= 0.55).

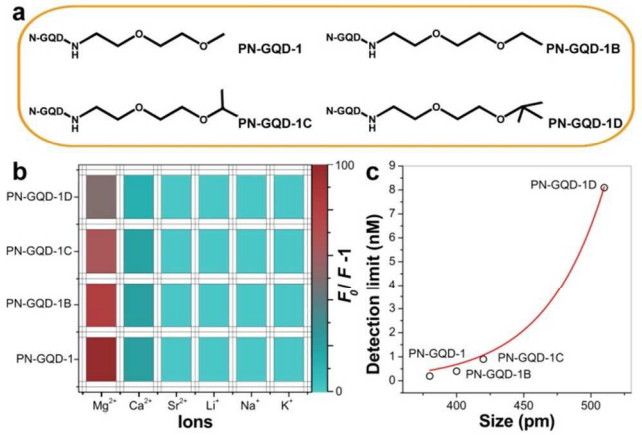

Figure 6 (a) molecular structures of PN-GQD-1 with different end group. (b) PL response of PN-GQD-1, PN-GQD-1B, PN-GQD-1C and PN-GQD-1D for different alkali and alkaline-earth metal ions. The concentration of PN-GQD-1 and ions is 0.2 mg mL^{-1} and 50 nM, respectively. (c) Relationship between the size of end groups and detection limit. The red curve shows the exponent fitting curve.

Moreover, we also discussed the effect of end group in polyether chains on the supramolecular recognition. Three kinds of PN-GQD-1 with different end groups (ethyl, isopropyl and tertiary butyl, corresponding to PN-GQD-1B, PN-GQD-1C and PN-GQD-1D, as shown in Figure 6a) were carried out. TEM images and PL spectrum are shown in Figure S9-11. The selectivity of PN-GQD-1, PN-GQD-1B, PN-GQD-1C and PN-GQD-1D show no obvious change (Figure 6b). When the concentration of corresponding ions is 50 nM, the dramatic PL quenching of PN-GQD-1, PN-GQD-1B, PN-GQD-1C and PN-GQD-1D can be observed. The PL intensity of PN-GQD-1, PN-GQD-1B, PN-GQD-1C and PN-GQD-1D decreased to the 0.9%, 1.2%, 1.6% and 2.0% of original intensity (F_0 / F -1 is 110, 82, 61 and 51, respectively), respectively. Meanwhile, on the other hand, the detection limit of PN-GQD-1, PN-GQD-1B, PN-GQD-1C and PN-GQD-1D change notably. As shown in Table 1, the detection limit of PN-GQD-1B, PN-GQD-1C and PN-GQD-1D is 0.4, 0.9 and 8.1 nM, respectively. Figure 6c shows the relationship between the size of end groups and detection limit. The detection limit shows exponential growth with size of end groups. The fitting formula is shown in E3 and the correlation coefficient (R^2) is 0.9962.

$L_d=8\times10^{-5}\times e^{(0.02255\times r)}$ (E3)

Where L_d is the detection limit (nM) of PN-GQDs. r is the size of end groups (pm). The fitting formula indicates the detection limit of PN-GQDs was strongly influence by the size of end groups. The increasing of L_d can be due to the steric hindrance of end groups. [56-60]

Finally, for potential applications, the photostability, antijamming capability and cytotoxicity of PN-GQDs were carried out. As sown in Figure S12, the PL intensity of PN-GQDs shows no obvious change under 150 W Xe lamp for 48 h. This indicates the PN-GQDs have excellent photostability. To evaluate the selectivity of these PN-GQDs fluorescent probe, we also examined the PL intensity changes in the presence of representative heavy metal ions under the same conditions, such as Zn^{2+}, Fe^{3+}, Ni^{2+}, Cd^{2+}, Cu^{2+}, Hg^{2+}, Pb^{2+}, Ag^{+}, Al^{3+} and Co^{2+} (Figure S13). No tremendous decrease was observed upon addition of other ions which indicates the excellent selectivity of PN-GQDs.

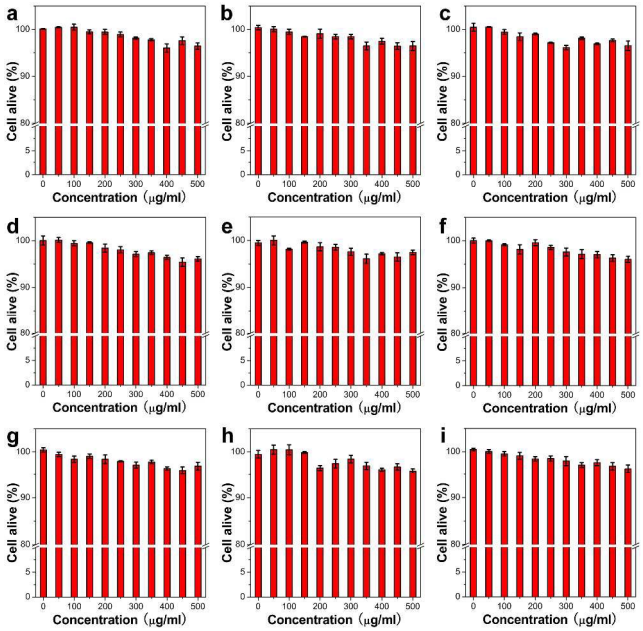

Figure 7 Metabolic activity of HeLa cells treated with different concentrations of (a) PN-GQD-1, (b) PN-GQD-2, (c) PN-GQD-3, (d) PN-GQD-4, (e) PN-GQD-5, (f) PN-GQD-6, (g) PN-GQD-1B, (h) PN-GQD-1C and (i) PN-GQD-1D.

For the *in vitro* cytotoxicity, the HeLa cell line is selected. The activity of HeLa cells treated with different concentrations of PN-GQD (Figure 7) was observed. Different concentrations of PN-GQD (0 to 500 μg mL^{-1}) were added to the cells cultured in 96 well-plates and incubated for 24 h. Subsequently, a standard assay was performed to assess the cell viabilities after the PN-GQD treatments. No significant reduction in cell viability was observed for cells treated with PN-GQD even at concentrations of up to 500μg mL^{-1}. These results indicated that PN-GQD could be used for intracellular imaging.

Conclusions

In summary, we demonstrated the tunable supramolecular recognition of PN-GQDs. The length of polyether chains decides the selectivity of PN-GQDs which conforms to logarithmic relationship with the ratio of charge to radius of ions. Meanwhile the detection limit shows exponential growth with end group size of polyether chains. The detection limit increased with the increased size of end groups which can be due to the steric hindrance of end groups. With tunable chain length of polyethylene glycol the PN-GQDs can be used as ultrasensitive and selective fluorescent probes for Li^+, Na^+, K^+, Mg^{2+}, Ca^{2+} and Sr^{2+}, respectively. The semiquantitative analyze for the supramolecular recognition of PN-GQDs is significant for the mechanism study and molecular designing of GQD based fluorescent probes.

Acknowledgements

This work was supported by projects from the Chinese Academy of Sciences (Grant no. KGZD-EW-303 and XDA02040000), and the Priority Academic Program Development of Jiangsu Higher Education Institutions on Renewable Energy Materials Science and Engineering.

Notes and references

State Key Laboratory of Functional Materials for Informatics, Shanghai Institute of Microsystem and Information Technology, Chinese Academy of Science, Shanghai, 200500, China.
E-mail: *gqding@mail.sim.ac.cn* (Guqiao Ding)

† Electronic Supplementary Information (ESI) available: [details of experiments, XPS survey spectra, FTIR spectra and PL properties of PN-GQDs]. See DOI: 10.1039/b000000x/

1. A. A. Lev, *Nature*, 1964, **201**, 1134.
2. S. W. Yang, J. Sun, X. B. Li, W. Zhou, Z. Y. Wang, P. He, G. Q. Ding, X. M. Xie, Z. H. Kang, M. H. Jiang, *J. Mater. Chem. A*, 2014, **2**, 8660.
3. F. Liao, X. Song, S. W. Yang, C. Y. Hu, L. He, S. Yan, G. Q. Ding, *J. Mater. Chem. A*, 2015, **3**, 7568.
4. J. A. Hinke, *Nature*, 1959, **184**, 1257.
5. F. Liao, S. W. Yang, X. B. Li, L. J. Yang, Z. H. Xie, C. S. Hu, S. Yan, T. Y. Ren, Z. D. Liu, *Synth. Met.*, 2014, **189**, 126.
6. T. Takami, J. W. Son, J. K. Lee, B. H. Park, T. Kawai, *Jap. J. Appl. Phys.*, 2011, **50**, 0813.
7. L. D. Faller, *Arch. Biochem. Biophys.*,2008, **12**, 476.
8. A. Y. Bagrov, J. I. Shapiro, O. V. *Fedrova, Pharmacol. Rev.*, 2009, **61**, 9.
9. I. Prassas, E. P. Diamandis, *Nat. Rev. Drug Discovery*, 2008, **7**, 926.
10. E. Neher, B. N. Sakmann, *Nature*, 1976, **260**, 799.
11. M. Tanha, S. K. Chakraborty, B. Gabris, A. S. Waggoner, G. Salama, D. Yaron, *J. Phys. Chem. A*, 2014, **118**, 9837.
12. J. C. Yu, L. Q. Zhang, X. Xu, S. Q. Liu, *Anal. Chem.*, 2014, **86**, 10741.
13. G. M. Cherf, K. R. Lieberman, H. Rashid, C. E. Lam, K. Karplus, M. Akeson, *Nat. Biotechnol.*, 2012, **30**, 344.
14. A. V. Doghaei, M. R. Housaindokht, K. Abnous, *Anal. Biochem.*, 2014, **466**, 72.
15. K. M. Modesto, J. E. Moller, W. K. Freeman, C. Shub, K. R. Bailey, P. A. Pellikka, *Am. J. Cardiol.*, 2006, **97**, 1247.
16. S. Yan, S. Yang, L. He, C. Ye, X. Song, F. Liao, *Synth. Met.*, 2014, **198**, 142.
17. Z. Chen, J. Guo, S. Zhang, L. Chen, *Sens. Actuat. B*, 2013, **188**, 1155.
18. Z. Chen, Y. Huang, X. Li, T. Zhou, H. Ma, H. Qiang, Y. Liu, *Anal. Chim. Acta*, 2013, **787**, 189.
19. H. He, M. A. Mortellaro, M. J. Leiner, R. J. Fraatz, J. K. Tusa, *J. Am. Chem. Soc.*, 2003 **125**, 1468.
20. T. T. Zhang, S. W. Yang, J. Sun, X. B. Li, L. He, S. Yan, X. Y. Kang, C. S. Hu, F. Liao, *Synth. Met.*, 2013, **181**, 86.
21. F. Liao, S. W. Yang, *Synth. Met.*, 2015, **205**, 32.
22. S. W. Yang, F. Liao, *Synth. Met*., 2012, **162**, 1343.
23. S. W. Yang, S. Q. Huang, D. Liu, F. Liao, *Synth. Met*., 2012, **162**, 2228.
24. D. Wang, J. F. Chen, L. M. Dai, *Part. Part. Syst. Charact.*, 2015, **32**, 515.
25. M. Bacon, S. J. Bradley, T. Nann, *Part. Part. Syst. Charact.*, 2014, **31**, 415.
26. Y. Q. Dai, H. Long, X. T. Wang, Y. M. Wang, Q. Gu, W. Jiang, Y. C. Wang, C. C. Li, T. Y. H. Zeng, Y. M. Sun, J. Zeng, *Part. Part. Syst. Charact.*, 2014, **31**, 597.
27. J. Sun, S. W. Yang, Z. Y. Wang, H. Shen, T. Xu, L. T. Sun, H. Li, W. W. Chen, X. Y. Jiang, G. Q. Ding, Z. H. Kang, X. M. Xie, M. H. Jiang, *Part. Part. Syst. Charact.*, 2015, **32**, 434.
28. L. Zhou, J. L. Geng, B. Liu, *Part. Part. Syst. Charact.*, 2013, **30**, 1086.
29. X. H. Zhu, X. Xiao, X. X. Zuo, Y. Liang, J. M. Nan, *Part. Part. Syst. Charact.*, 2014, **31**, 801.
30. H. Kobayashi, M. Ogawa, R. Alford, P. L. Choyke, Y. Urano, *Chem. Rev.*, 2010, **110**, 2620.
31. R. Gokhale, P. Singh, *Part. Part. Syst. Charact.*, 2014, **31**, 433.
32. S. W. Yang, C. Zhu, J. Sun, P. He, N. Y. Yuan, J. N. Ding, G. Q. Ding, X. M. Xie, *RSC Adv.*, 2015,**5**, 33347.
33. S. W. Yang, J. Sun, P. He, X. X. Deng, Z. Y. Wang, C. Y. Hu, G. Q. Ding, X. M. Xie, *Chem. Mater.*, 2015, **27**, 2004.
34. J. J. Liu, X. L. Zhang, Z. X. Cong, Z. T. Chen, H. H. Yang, G. N. Chen, *Nanoscale*, 2013, **5**, 1810.
35. L. L. Li, G. H. Wu, G. H. Yang, J. Peng, J. W. Zhao, J. J. Zhu, *Nanoscale*, 2013, **5**, 4015.
36. P. H. Luo, Z. Ji, C. Li, G. Q. Shi, *Nanoscale*, 2013, **5**, 7361.
37. G. S. Kumar, R. Roy, D. Sen, U. K. Ghorai, R. Thapa, N. Mazumder, S. Sahab, K. K. Chattopadhyay, *Nanoscale*, 2014, **6**, 3384.
38. S. W. Yang, S. Q. Huang, D. Liu, F. Liao, *Synth. Met.*, 2012, **162**, 2228.
39. S. W. Yang, F. Liao, *Synth. Met.*, 2012, **162**, 1343.
40. X. B. Li, S. W. Yang, J. Sun, P. He, X. G. Xu, G. Q. Ding, *Carbon*, 2014, **78**, 38.
41. X. B. Li, S. W. Yang, J. Sun, P. He, X. P. Pu, G. Q. Ding, *Synth. Met.*, 2014, **194**, 52.
42. X. Song, S. W. Yang, L. He, S. Yan, F. Liao, *RSC Adv.*, 2014, **4**, 49000.
43. P. He, J. Sun, S. Y. Tian, S. W. Yang, S. J. Ding, G. Q. Ding, X. M. Xie, M. H. Jiang, *Chem. Mater.*, 2015, **27**, 218.
44. C. Zhu, S. W. Yang, G. Wang, R. W. Mo, P. He, J. Sun, Z. F. Di, Z. H. Kang, N. Y. Yuan, J. N. Ding, G. Q. Ding, X. M. Xie, *J. Mater. Chem. B*, 2015, **3**, 6871.
45. C. Zhu, S. W. Yang, G. Wang, R. W. Mo, P. He, J. Sun, Z. F. Di, Z. H. Kang, N. Y. Yuan, J. N. Ding, G. Q. Ding, X. M. Xie, *J. Mater. Chem. C*, 2015, **3**, 8810.
46. S. H. Hu, Y. W. Chen, W. T. Hung, I. W. Chen, S. Y. Chen, *Adv. Mater.*, 2012, **24**, 1748.
47. H. Tetsuka, R. Asahi, A. Nagoya, K. Okamoto, I. Tajima, R. Ohta, A. Okamoto, *Adv. Mater.*, 2012, **24**, 5333.
48. T. E. Kaiser, H. Wang, V. Stepanenko, F. Wurthner, *Angew. Chem., Int. Ed.*, 2007, **46**, 5541.
49. F. Wang, Z. Xie, H. Zhang, C. Liu, Y. Zhang, *Adv. Funct. Mater.*, 2011, **21**, 1027.
50. F. Liao, S. Yang, X. Li, S. Yan, C. Hu, L. He, X. Kang, X. Song, T. Ren, *Synth. Met.*, 2014, **190**, 7985.
51. M. Rahman, H. J. Harmon, *Spectrochim. Acta, Part A*, 2006, **65**, 901.
52. F. Liao, S.W. Yang, X. B. Li, L. J. Yang, Z. H. Xie, C. S. Hu, L. He, X. Y. Kang, X. Song, T. Y. Ren, *Synth. Met.*, 2014, **189**, 135.
53. W. W. Qin, M. Baruah, M. Sliwa, M. V. Auweraer, W. M. D. Borggraeve, D. Beljonne, B. V. Averbeke, N. Boens, *J. Phys. Chem. A*, 2008, **112**, 6104.
54. M. Baruah, W. W. Qin, R. A. L. Valle, D. Beljonne, T. Rohand, W. Dehaen, N. Boens, *Org. Lett.*, 2005, **7**, 4377.
55. N. Boens, V. Leen, W. Dehaen, *Chem. Soc. Rev.*, 2012, **41**, 1130.
56. X. Q. Chen, Y. Zhou, X. J. Peng, J. Yoon, *Chem. Soc. Rev.*, 2010, **39**, 2120.
57. W. Lu, X. Qin, S. Liu, G. Chang, Y. Zhang, Y. Luo, A. M. Asiri, A. O.

Al-Youbi, X. Sun, *Anal. Chem.*, 2012, **84**, 5351.
58. X. Qin, W. Lu, A. M. Asiri, A. O. Al-Youbi, X. Sun, *Catal. Sci. Technol.*, 2013, **3**, 1027.
59. H. Li, J. Zhai, X. Sun, *RSC Adv.*, 2011, **4**, 725.
60. S. Liu, J. Tian, Wang, Y. Zhang, X. Qin, Y. Luo, A. M Asiri, A. O Al-Youbi, X. Sun, *Adv. Mater.*, 2012, **24**, 2307.